Emulsified and liquid-liquid phase separated states of α-pinene secondary organic aerosol determined using aerosol optical tweezers

Kyle Gorkowski,[1] Neil M. Donahue,[1] Ryan C. Sullivan[1,*]

[1]Center for Atmospheric Particle Studies, Carnegie Mellon University, Pittsburgh, PA, 15213

*Corresponding Author: Ryan C. Sullivan; rsullivan@cmu.edu

Abstract

We demonstrate the first capture and analysis of secondary organic aerosol (SOA) on a droplet suspended in an aerosol optical tweezers (AOT). We examine three initial chemical systems of aqueous NaCl, aqueous glycerol, and squalane at ~75% relative humidity. For each system we added α-pinene SOA – generated directly in the AOT chamber – to the trapped droplet. The resulting morphology was always observed to be a core of the original droplet phase surrounded by a shell of the added SOA. We also observed a stable emulsion of SOA particles when added to an aqueous NaCl core phase, in addition to the shell of SOA. The persistence of the emulsified SOA particles suspended in the aqueous core suggests that this metastable state may persist for a significant fraction of the aerosol lifecycle for mixed SOA/aqueous particle systems. We conclude that the α-pinene SOA shell creates no major diffusion limitations for water, glycerol, and squalane core phases under humid conditions. These experimental results support the current prompt-partitioning framework used to describe organic aerosol in most atmospheric chemical transport models, and highlight the prominence of core-shell morphologies for SOA on a range of core chemical phases.

Abstract Art

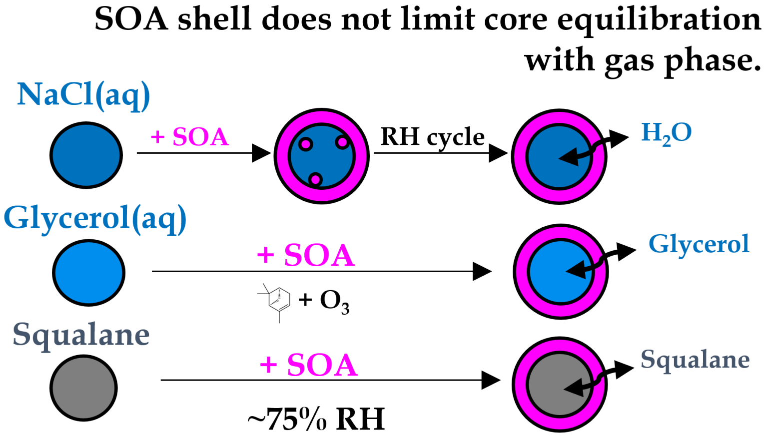

KEYWORDS: atmospheric chemistry, organic aerosol, Raman spectroscopy, optical tweezers, whispering gallery modes, phase separations, particulate matter

Introduction

Atmospheric particulate matter is a complex mixture of organic carbon, elemental carbon, and inorganic, metallic, and mineral components, all mixed with a variable amount of water[1,2]. Organic aerosols arise from direct emissions of primary organic aerosol (POA) and from oxidation of precursors – VOCs and evaporated POA – that generates less-volatile secondary organic aerosol (SOA)[3,4]. Complex SOA is a major component of atmospheric organic aerosol, constituting between 30-70% of the total aerosol mass[4,5]. It is composed of thousands of individual organic compounds[6–8]. SOA is a major component of particulate matter, which affects human health and climate change[9,10]. Aerosol optical tweezers (AOT) provide a new analytical technique to explore the composition and the thermodynamic properties of this complex material using isolated suspended droplets and cavity-enhanced Raman spectroscopy.

Liquid particles are common under atmospheric conditions. Depending on the constituents, they can undergo phase separation into distinct chemical phases[11–17]. We broadly categorize these liquid particles as either homogeneously mixed single-phase structures or liquid-liquid phase separated (LLPS) structures[15,18–21]. For a phase-separated particle, the two predominant equilibrium states are a core-shell or partially-engulfed arrangement of the phases[19,22–24]. There is also visual evidence from optical microscopy that phase-separation can result in multiple inclusions forming on or in the aqueous phase, producing a complex morphology[25,26]. Recent work by Altaf and Freedman[27] has shown that under atmospheric conditions there is a size dependent transition such that particles remain in a homogeneous morphology when they are <50 nm in diameter[27–29]. Their observation supports applying the results of phase-separation studies, like this one, to atmospheric particles > 50 nm. The cavity-enhanced Raman spectrum retrieved from a droplet trapped in an AOT instrument provides a unique and real-time morphology measurement that can distinguish between these three structures in mixed droplets[30–32].

Particle morphology is important. The composition at the air-particle interface dictates the particle's ability to undergo chemical reactions with gas-phase reactants and controls the rates and mechanisms of those reactions[33,34]. N_2O_5 is a key reservoir of nitrogen oxides that demonstrates the importance of this air-particle interface. The reactive uptake coefficient of N_2O_5, $\gamma(N_2O_5)$, governs the N_2O_5 nocturnal removal rate from the atmosphere *via* hydrolysis in aqueous aerosol phases, and a hydrophobic shell on an aqueous core substantially reduces the probability of the reactive uptake[35,36]. Reactive uptake also increases aerosol mass loadings through aqueous chemistry, for example with isoprene-derived SOA[37,38].

Using smog-chamber experiments, Ye et al.[39] showed that the Hansen solubility framework could inform the miscibility of α-pinene SOA into pure component seeds. The general result from these smog-chamber mixing experiments is that highly polar and nonpolar phases do not mix with SOA, while SOA does dissolve into phases of intermediate or mixed polarity. These techniques used in smog-chamber experiments can infer phase separation from changes in the aerosol mass yield, aerosol size distribution, or the mixing state of components measured using single-particle analysis, but are unable to determine the critical information regarding the resulting particle morphology[7,39–41]. For a core-shell morphology, diffusion through the shell could dictate the equilibration rates of molecules partitioning into or out of the particle-phase[42–46]. This shell effect would not be present in a partially-engulfed morphology.

Here we report the first AOT experiments on complex SOA, extending our current understanding regarding the phase separation of SOA using the AOT's ability to distinguish between the three equilibrium morphologies: phase-separated core-shell and partially-engulfed structures, and homogeneous single-phase structures[15,20,24,30,32,47]. Furthermore, we can observe in real-time any changes in the droplet's morphology while its composition changes[32,48,49]. The AOT isolates individual micron-sized droplets freely suspended in air and avoids interference from contact with a surface. It does not require collection of the aerosol onto a substrate followed by solvent extraction required by other methods[12,32,50,51].

Experimental Methods

In situ Ozonolysis of α-pinene in the Aerosol Optical Tweezers

Our AOT system was previously described and characterized by Gorkowski et al. [32]. Briefly, a 532 nm laser passes through a set of expansion lenses overfilling the back aperture of a 100x (NA 1.25) oil immersion objective. The objective presses against the bottom of a thin glass coverslip, and an optical gradient force trap forms approximately 40 microns above the coverslip inside the AOT chamber. To generate glycerol and squalane droplets we use a Condensational Monodisperse Aerosol Generator (CMAG; TSI, Inc.) and to generate NaCl(aq) droplets we use a medical nebulizer (PARI TREK S). We control the relative humidity (RH) in the chamber by varying the flow ratio of dry to humidified air and we measure RH at the inlet using a hygrometer (Vaisala).

Previous AOT work by Dennis-Smither et al.[47] used direct ozonolysis of a trapped oleic acid droplet, a proxy for primary organic aerosol; we extended the AOT technique to determine the properties and chemistry of SOA produced from the oxidation of precursor vapors. We used dark ozonolysis of α-pinene vapor to produce SOA directly inside the AOT chamber from the formation of less-volatile oxidation products, some of which homogeneously nucleated to form particles. The gas and particle-phase products then collided with the trapped particle, modifying its composition. A diagram of the experimental setup and a detailed description of the procedural methods are provided in the Supplemental Information.

During a typical ozonolysis experiment, the ozone concentration in the AOT is 55 ppm_v, and the α-pinene vapor concentration is 500 ppm_v, based on the saturated vapor pressure of α-pinene and volumetric flow rates. The ozonolysis of α-pinene proceeds by addition of O_3 to the lone double bond and the reaction is ozone limited under these conditions[52]. This decomposition of the resulting Criegee intermediate goes on to produce ·OH radicals with a yield of ~0.8; under our conditions essentially all of the ·OH reacts with α-pinene[52]. Consequently, the SOA consists of an approximately 0.8:1 mixture of ·OH and ozone oxidation products. We occasionally observe nucleation of detectable particles from the α-pinene oxidation in the form of small-particle light scattering events in the tweezed droplet's visual image. The SOA vapors and particles are produced in the upper section of the AOT chamber and then flow down to the tweezed droplet at the bottom of the AOT chamber. The metal chamber walls do adsorb some of the less volatile SOA components, but these components by necessity are also present in the nucleated particles that coalesce with the tweezed droplet[53].

Raman Spectrum Analysis of Core-Shell Droplets

We use a spectrograph to record Raman scattering from the tweezed droplet, including resonant whispering gallery modes (WGMs). At the wavelength of each WGM, the droplet acts as a high finesse optical cavity where the WGMs form a standing wave near the droplet surface, amplifying the Raman scattering[54,55]. Any radial inhomogeneities in the droplet will weaken the amplification of the WGMs. For partially-engulfed morphologies the WGM amplification process is completely quenched[20,47]. The WGM amplification process will remain for core-shell morphologies as it is radially symmetric[15,32].

To distinguish the morphology of a core-shell versus a homogeneous droplet, we use a Mie scattering algorithm based off the one developed by Preston and Reid[56,57]. When applied to a core-shell droplet we use the plausibility of the retrieved effective refractive index and diameter parameters as well as an abnormally high fit error to identify a droplet with a core-shell morphology[15,32]. Fitting WGMs of a core-shell droplet to a homogeneous Mie model results in a consistently high fit error. To assess whether the core-shell morphology is valid we have developed a fitting algorithm for the WGMs from a core-shell morphology that retrieves the diameter and effective refractive index of both the core and shell phases, separately. Both the homogeneous and core-shell fit only retrieve the real part of the effective refractive index. We provide an accuracy characterization for the core-shell fitting in the Supplemental Information and will fully describe the fitting algorithm in a subsequent manuscript.

Results

Emulsions and Coatings of SOA on an Aqueous Inorganic Droplet

SOA and SOA mimics have been observed to phase separate from an aqueous inorganic phase in large droplets examined visually on microscope slides[14,17,58]. We performed experiments in the AOT on similar systems composed of SOA mixed with aqueous NaCl to determine the conditions under which SOA phase separates from aqueous phases. We determined the resulting droplet morphology using the cavity-enhanced Raman spectrum retrieved by the AOT and thus avoided interference through contact with any surface.

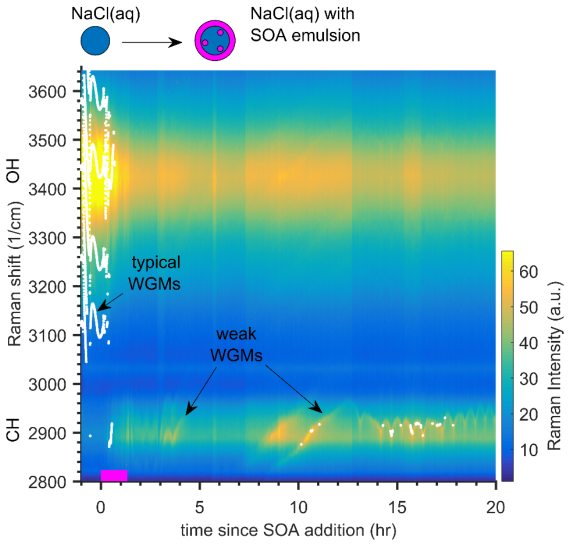

Figure 1. Raman spectral time series for a tweezed aqueous NaCl droplet before, during (pink bar at the bottom), and after α-pinene SOA was generated *in situ*, at 78% RH. The C-H hydrocarbon Raman mode center is at 2900 cm^{-1}, the O-H water mode is at 3450 cm^{-1}, and the color scale indicates the intensity of the Raman signal at that Raman shift position. The bright white points indicate the positions of detectable WGMs. The SOA flow reaction started at 0 min and lasted for 1.3 hr, indicated by the pink bar. The weak WGMs following the SOA addition are visible by eye but remain below our peak detection limit for 48 hours; only the first 20 hours are shown here. The small waves (with a period of ~0.5 hr) in the WGMs after 14 hr are caused by small temperature/humidity fluctuations (~1% RH) due to the laboratory's HVAC system.

In Figure 1 we show data from an experiment in which we added SOA generated *in situ* to a tweezed NaCl(aq) droplet beginning at 0 minutes. We observe typical WGM resonances in the Raman spectrum in the broad O-H water stretch region before the SOA addition ($t \leq 0$ min); these correspond to a homogeneous morphology. The droplet's size was 7.308 ± 0.001 µm, and its effective refractive index ($n_{650\text{nm}}$) was 1.380 ± 0.0015 just before SOA addition. During and after the SOA addition, Raman scattering appears in the C-H hydrocarbon region due to the uptake of organic carbon, and weak WGMs are present in both the O-H and C-H Raman regions. The WGMs are weaker following SOA addition but still faintly visible in the Raman spectrum's time series; their intensity is diminished but not completely quenched.

The persistence of weak WGMs following addition of SOA to an aqueous NaCl drop means we cannot conclude that the mixed droplet formed a partially-engulfed structure, because that would completely quench the WGMs. Theoretical modeling of a spherical droplet with an emulsion showed that as the number of emulsified particles increased the WGMs are weakened and become broader[59]. Experiments using an electrodynamic balance showed that adding polystyrene latex spheres (d_p of 30, 64, or 105 nm) to a supermicron glycerol droplet weakens the WGM signal[60]. The heterogeneities in the radial path of the resonating wavelengths of light would scatter the resonating WGM and intermittently quench the WGM signal. Some possible configurations of these heterogeneities are shown in the supplemental information; they are all classified as a type of emulsion. As we observe some WGM amplification, we propose that the droplet consists of a homogeneous SOA shell coating a supermicron aqueous NaCl core containing emulsified SOA particles retained during the coalescence of SOA particles onto the tweezed droplet. Along with the emulsion, the more polar compounds in the SOA are water soluble, so a small fraction of the SOA should also dissolve into the aqueous phase. Two-dimensional microscopy images in the literature support this proposed shell phase with an emulsion of SOA in an aqueous core[14,17,58]. However, it is difficult to resolve the 3-dimensional morphology from those microscopy images because they only show one viewing angle. This is not a limitation of the AOT. In the Supplemental Information, we demonstrate that radial heterogeneities can weaken the WGM amplification by coagulating NaCl crystals onto a trapped squalane droplet. This further supports our SOA emulsion interpretation of the Raman spectrum in Figure 1.

To further test our emulsion hypothesis, we waited for 48 hours (the first 20 hours are shown in Figure 1) to see if the emulsion would relax (Ostwald ripening) since emulsified particles represent a metastable state[61]. We continued the flow of humidified clean air to maintain the aqueous phase, so semi-volatile SOA should have evaporated to some extent from the droplet. The relatively stable WGM positions with time (Figure 1, 10 to 20 hours) shows that the droplet diameter remained nearly constant, indicating the remaining SOA did not evaporate to a noticeable extent.

In a second experiment on the same SOA + NaCl(aq) aerosol system, we used an RH cycle on the emulsified core-shell droplet to test the effect of dehydrating the aqueous core (which presumably contained the emulsified particles), as this might promote demulsification. The Raman spectrum and extracted WGMs positions measured in this experiment are shown in the bottom of panel of Figure 2 and the effective refractive indexes and diameters fit from the WGM positions are shown in the top two panels. We use the homogeneous fit error (blue/green bar in Figure 2) and inconsistent fit parameters to indicate an invalid homogeneous fit result. The initial aqueous NaCl droplet was 8.522 ± 0.001 µm with an $n_{650\mathrm{nm}}$ of 1.376 ± 0.0015, after which we added the SOA. We subsequently cycled the RH from 80% down to 55% and then back up to 79% (Figure 2). After the RH decreased at 224 min, 4 or 6 relatively strong WGMs appeared in the spectrum. The spectra during the drier period also exhibit more typical WGM amplification. After we increased the RH back up to 79% at 235 min, the strong WGMs typical of a homogeneous spherical geometry intensified, with 6 or more strong WGMs visible in a 2-second frame. Isolated Raman spectra covering this transition period are provided in the Supplemental Information.

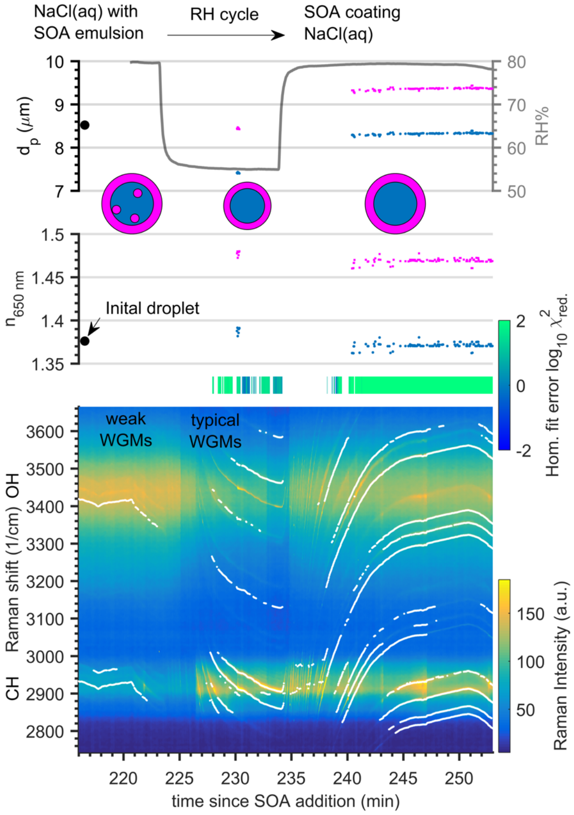

Figure 2. Raman spectra time series for a tweezed aqueous NaCl droplet after coagulation with α-pinene SOA, undergoing a relative humidity (RH) cycle. The bottom graph is the time series of the Raman spectra, the middle is the refractive index at 650 nm, and the top is the droplet diameter (left axis) and conditioned air's relative humidity (right axis). The time series started after the α-pinene SOA addition which happened at 0 min. and lasted for 65 min. The initial homogeneous NaCl droplet fit results are shown as black circles. WGMs that meet the peak criteria are shown as white points/lines in the Raman spectral time series. The fit error for the homogeneous morphology model is shown in the green/blue bar, where consistently green indicates an invalid fit to the homogeneous model. The fitted core-shell droplet diameter and refractive index are shown above for both the core (blue dots) and shell (pink dots) phases. The retrieved $n_{650\text{nm}}$ values are consistent with a core of NaCl(aq) and a shell of α-pinene SOA. The morphologies we infer during this experiment are displayed where an emulsion of SOA in the aqueous core is relaxed to a core-shell morphology via the RH cycle.

When we fit the WGMs after the RH cycle with the homogeneous Mie model appropriate for a single phase, the results are inconsistent and have high fit error,

$\log_{10}(\chi^2_{red}) > 0$ (blue/green bar in Fig. 2). When we fit the WGMs using the core-shell Mie model the results are consistent with what we would expect based on the initial conditions, the RH cycling, and the starting droplet size, shown in Figure 2. The refractive index of the α-pinene SOA shell ($n_{650\text{nm}}$ = 1.469 ± 0.004) is well within the range reported in the literature ($n_{532\text{nm}}$ = 1.39-1.52); see the Supplemental Information for a comparative table[62–66]. The core refractive index, $n_{650\text{nm}}$, of 1.372 ± 0.005 is within the uncertainty of the initial droplet ($n_{650\text{nm}}$ = 1.376 ± 0.0015), suggesting that no measurable SOA dissolved into the core. The solution has an NaCl mole fraction of 0.16, calculated via E-AIM[8,67]. By using a volume fraction mixing rule we estimated the maximum amount of SOA that could dissolve and still be within the error of our fit. For the core refractive index this means the volume fraction of SOA in the core is less than 4.3%. The droplet size is quite stable, as shown in the figure; though the WGM positions after the RH cycle at 235 min do change with time, 1 cm^{-1} corresponds to roughly 2 nm in diameter, so the growth is a fraction of a micrometer. The core-shell fit results support a morphology where α-pinene SOA coats the NaCl(aq) core. Based on these results we conclude that coalescence of submicron SOA particles onto a high ionic strength aqueous NaCl droplet results in a droplet coated with a spherical shell but containing emulsified SOA particles as well. The subsequent RH cycle causes the droplet to assume an equilibrium core-shell morphology with an SOA shell, no residual emulsified SOA, and little dissolved SOA.

Morphology of an Aqueous-Organic Mixed Droplet

A natural extension of SOA coalescence to an aqueous inorganic core is SOA coalescence to an aqueous-organic core. In this way, we can isolate the role of water in the phase separation and remove the salting out effect of the relatively high ionic strength aqueous inorganic solution. We use glycerol as it is hygroscopic and is active in both the C-H and O-H Raman modes.

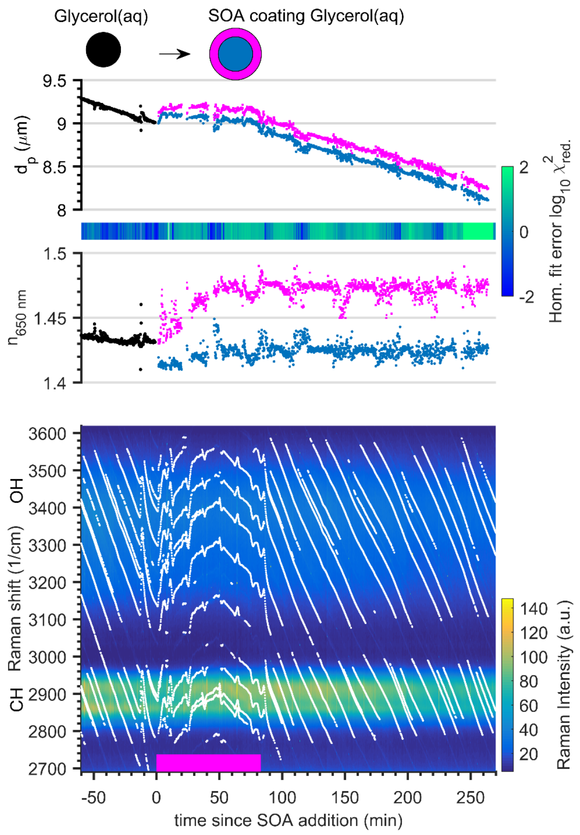

Figure 3. Raman spectral time series for a tweezed aqueous glycerol droplet with the addition of α-pinene SOA, at 73% RH. Raman spectra are shown in the bottom graph, and the white points indicate the positions of detectable whispering gallery modes (WGMs). The decreasing slope of the WGM traces indicates the droplet is evaporating. The α-pinene SOA flow reaction started at 0 min. and lasted for 80 min., indicated by the pink bar. The droplet's refractive index and diameter retrieved from the WGM analysis are shown in the middle and top panels. The fit results of the WGM positions to a homogeneous Mie model are in the top two plots as black dots. The fit error for the homogeneous model is shown in the green/blue bar, where consistently blue indicates a valid fit and green indicates an invalid fit to the model. The core-shell fitting is then used to retrieve the properties of the glycerol(aq) core (blue points) and the α-pinene SOA shell (pink points) after SOA generation started at 0 min.

We trapped a glycerol droplet at 73% RH, finding $n_{650\mathrm{nm}}$ of 1.4314 ± 0.0013 with a homogeneous Mie model. In Figure 3 it is apparent that, before the α-pinene SOA addition at t = 0, the droplet was shrinking rapidly. The retrieved diameter and the negative slope of the WGM positions indicate evaporation of the glycerol (water volume fraction should remain constant because of the constant RH). When we added α-pinene SOA to the droplet, the homogeneous Mie fitting of the WGMs failed immediately, as indicated by the increased fit error of the homogeneous model. However, the core-shell Mie model could successfully fit the WGMs both during and after the SOA addition. The core-shell refractive index results indicate that a shell of α-pinene SOA ($n_{650\text{nm}} = 1.474 \pm 0.005$) coated the glycerol(aq) core ($n_{650\text{nm}} = 1.4325 \pm 0.007$). The refractive index of the SOA shell is consistent with the NaCl(aq) experiment described above and within the literature range (summarized in the Supplemental Information). As with the high ionic strength NaCl(aq) droplet, we observed no measurable dissolution of the SOA into the aqueous organic core; the volume fraction of SOA in the aqueous glycerol solution was < 17% based on the measured $n_{650\text{nm}}$. In contrast to the NaCl(aq) system, we do not observe evidence of an emulsion, as strong WGMs persisted throughout the experiment.

The continued evaporation of the core indicates that the α-pinene SOA did not prevent or retard evaporation of glycerol from the core. The measured evaporation rate for the glycerol(aq) core decreased by 22% after we added the α-pinene SOA. This decrease may be due to Raoult's Law of SOA mixing in the glycerol(aq) core depressing the overall evaporation rate of the core. That decrease could also be due to a diffusion limitation of glycerol through the SOA shell. If the SOA dissolved in the core was at our upper limit of 17% by volume, Raoult's Law could explain the majority of the decrease in evaporation rate. We will systematically explore these confounding effects of mixing and diffusion limitations in the glycerol plus SOA system in future experiments by varying the amount of SOA added to the droplet. One thing that is clear from this experiment is that the SOA shell does not trap glycerol in the SOA phase and does not prevent glycerol from partitioning to the gas phase.

We can also use the evolution of the shell thickness, as shown in Figure 3, to calculate the evaporation rate and thus the effective vapor pressure of the SOA shell. To do this, we calculated the volume loss of the shell for the period between 160 min. and

260 min. and assumed an SOA molecular weight of 300 g/mol and a density of 1.4 g/cm^3 [68–70]. There was very little evaporation, and so the effective vapor pressure of the SOA shell was 5.2×10^{-6} Pa or equivalently a C^* of 0.64 µg/m^3 ($10^{-0.193}$ µg/m^3)[48,53,71,72]. This retrieved volatility is higher due to our high precursor conditions than the measurements made during the α-pinene SOA evaporation experiment described by Yli-Juuti et al.[73], with $C^* \simeq 10^{-3}$ µg/m^3 at 80% RH. Lastly, in contrast to typical SOA evaporation experiments, our shell phase does not appear to contain a large portion of intermediate-volatile organic carbon with higher C^* values as the evaporation rate we observed was constant. This could be due to additional aqueous chemistry of the SOA at the aqueous-core interface, leading to lower volatility SOA in the shell phase[74].

Morphology of SOA Added to a Hydrophobic Organic Droplet

Having studied two aqueous cores, next we studied the mixing of SOA with a tweezed hydrophobic squalane ($C_{30}H_{62}$) droplet. Our objective was to replicate the chemical system studied in a smog-chamber mixing experiment conducted by Robinson et al.[7]. They studied the same particle system by condensing α-pinene ozonolysis SOA onto squalane seed particles and also condensing squalane vapors from a heated injector onto SOA particles. After increasing the chamber temperature by 22 °C, they observed rapid evaporation of the squalane and little evaporation of the SOA. They also found that squalane and α-pinene SOA remained phase-separated during a particle mixing experiment. Based on these experiments they concluded that the mixed particles formed a two-phase morphology, noting that if the particles had a core-shell morphology with the squalane forming the core, the evaporating squalane would have to diffuse relatively rapidly through the SOA shell. That single-particle smog-chamber experiment could not fully constrain the phase-separated particle morphology, leaving the hypothesis that squalane can diffuse rapidly through SOA unproven. If the morphology were partially-engulfed, then squalane would have direct access to the gas phase. The aerosol optical tweezers provide a unique way to determine the morphology of this complex system directly.

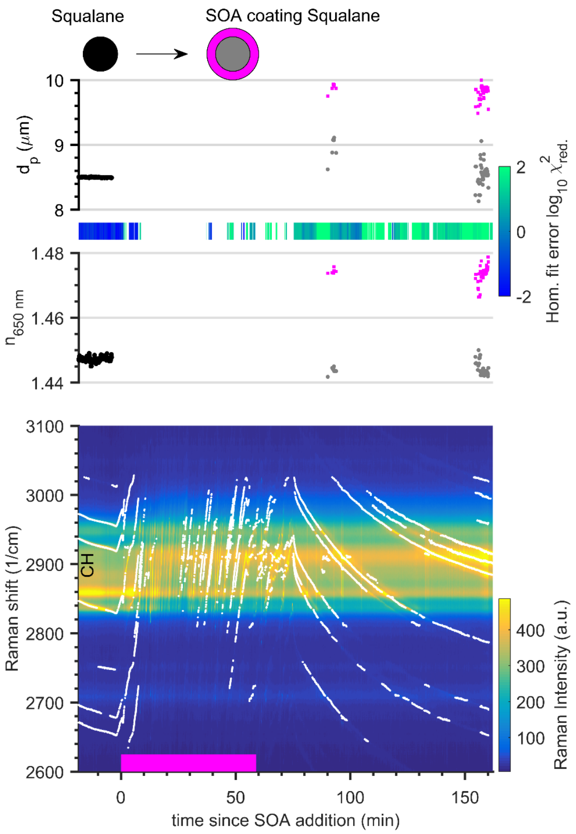

Figure 4. Raman spectral time series for a tweezed squalane droplet and addition of α-pinene SOA, at 80% RH, following the same format as in Fig. 3. A decreasing trend of the WGM traces indicates the droplet was evaporating whereas an increase indicates droplet growth. The α-pinene SOA addition started at 0 min. and lasted for 60 min., indicated by the pink bar. The fit results of the WGM positions to a homogeneous model are shown in the top two plots as black dots. The core-shell fitting model is then used to retrieve the properties of the squalane core (gray) and α-pinene SOA shell (pink) following SOA addition. Few WGMs are retrieved as the C-H hydrocarbon band is too narrow to consistently contain at least 6 WGMs that are required for the core-shell Mie fit.

In Figure 4 we show spectra from an experiment starting with a pure squalane droplet, with an initial diameter of 8.492 ± 0.004 µm and a refractive index, $n_{650\text{nm}}$, of 1.447 ± 0.001, to which we added α-pinene SOA by coagulation. The WGMs were initially almost horizontal, with a slight negative slope due to the slow evaporation of squalane, which has an estimated vapor pressure of 1.93×10^{-6} Pa[75]. When we began to add α-pinene SOA, the WGM slopes became strongly positive, indicating that the particle was growing. The persistence of the WGMs also indicates that the SOA spread rapidly across the squalane surface as it condensed and coagulated, excluding a partially-engulfed morphology. After the α-pinene SOA addition at 70 min., we held the chamber static with all airflows off before turning on clean airflow at 80 min.; the droplet then began to shrink, indicated by the negative slope of the WGMs. The fit results for the core-shell droplet are sparse because the droplet contains mostly C-H bonds, which have a narrow Raman band reducing the number of WGMs observed. However, the few fits are consistent with a squalane core coated by SOA. Moreover, the slope of the WGMs at the end of the experiment is similar to the slope at the beginning, suggesting that slow squalane evaporation (few nm per minute) dominates the particle evolution. The slightly higher slope soon after the SOA addition also suggests that some SOA evaporated from the shell.

Consistently high homogeneous Mie fit error following the addition of α-pinene SOA indicates that the droplet was not homogeneous, while the persistence of the WGMs rules out a partially–engulfed morphology. Based on this evidence we conclude that the droplet was phase separated, which is consistent with the smog-chamber studies[7,39]. Our AOT results add the additional insight that the particle morphology is core-shell with α-pinene SOA coating squalane. This direct measurement of the morphology is inaccessible from traditional smog-chamber observations of a large ensemble of particles. The core refractive index, $n_{650\mathrm{nm}}$, of 1.444 ± 0.003 and diameter of 8.577 ± 0.186 μm provide evidence that no measurable amount of SOA was dissolved into the core (volume fraction < 11%). The retrieved refractive index of the α-pinene SOA shell ($n_{650\mathrm{nm}}$ = 1.473 ± 0.003) is consistent with the previous two experiments on aqueous NaCl and glycerol.

Note that squalane lacks any unsaturated bonds for ozone to attack. Squalane can be oxidized by the ·OH radicals produced by the ozonolysis of α-pinene, but this heterogeneous oxidation would be much slower than the gas-phase oxidation of α-pinene by ·OH due to mass transfer limitations from the gas phase to particle interface[76]. The squalane core also quickly became protected by the SOA coating.

Discussion

Our extension of the AOT technique to generate and study complex α-pinene SOA *in situ* enables real-time investigations of complex aerosol systems at the individual particle level that more realistically mimic atmospheric aerosol compositions. Fitting of the WGMs provides highly accurate measurements of the droplet's size and refractive index that allow us to determine how different droplet compositions respond to the addition of SOA. These AOT experiments on *in situ* generated α-pinene SOA avoid limitations intrinsic to other measurements of phase separation and morphology using SOA filter extracts, where the solvent can alter the composition and only recovers the soluble portion, such as the water-soluble fraction of SOA[25,77–79].

The mixing experiments on aqueous organic, aqueous inorganic, or hydrophobic organic particle phases with SOA all resulted in a liquid-liquid phase separation, demonstrating that phase separation is common for the aerosol mimics probed here. We also add further evidence to indicate that core-shell morphologies are common structures for complex mixed atmospheric aerosol mimics[21,80]. Our work here focused on high humidity ranges of 70% to 80% RH to isolate the effect of the starting droplet composition; in future work, we will explore the effect of RH on the resulting phase-separated morphology.

The high precursor concentrations used here are not representative of the ambient troposphere, and as such may affect our resulting SOA oxidative state and volatility. This high precursor effect appears to have shifted our SOA volatilty higher as our measured SOA volatility was greater than observed in an evaporation experiment by Yli-Juuti et al. [73]. The higher volatility SOA products that partitioned to the particle phase would likely result in a lower viscosity[81]. More volatile SOA products are typically less oxidized, and the less polar nature of these molecules reduces the strength of the inter-molecular interactions they experience, reducing their viscosity while increasing their volatility.

Through the core-shell fitting of our different SOA systems, we also retrieve the refractive index to a 0.4% accuracy. Our retrieved refractive index is valuable as previous optical closure studies on SOA systems yielded a wide range of refractive indices Table S2). The variability is in part due to the methods used where a new volume of particles is measured at each data point. In the AOT the environment is more controlled, and we measure the properties of the same SOA mass in real-time, which reduces experimental variability between measurements.

Synthesizing the results from the different RH stages of the aqueous NaCl droplet plus SOA experiment strengthens our proposal for the emulsion of SOA particles in the aqueous core. Dehydration of the aqueous core demulsified the SOA and produced a stable irreversible core-shell morphology of SOA coating the NaCl(aq). From this, we can conclude that the core-shell morphology observed is the thermodynamically stable condition for this mixed system, and the emulsion was metastable. Therefore, before the RH cycle, it is likely that a core-shell morphology was thermodynamically favored then as well. Finally, a droplet morphology composed of a homogenous SOA shell and the inhomogeneous core of emulsified SOA particles in aqueous NaCl would also explain the diminished WGM amplification observed. This homogeneous shell and inhomogeneous core would account for the resonance of WGMs in the surface layer of the SOA shell, while not permitting the full amplification of the WGMs due to interference by the emulsion in the core. The prompt collapse of the emulsified state following the decrease in RH suggests a chemical rather than physical explanation for the rapid demulsification. The increase in the ionic strength of the NaCl(aq) core caused by its partial dehydration (Fig. 2) would significantly change the interfacial energies between the SOA and NaCl(aq) phases. This likely caused the emulsified SOA particles to destabilize and the organic material to largely partition to the SOA shell around the NaCl(aq) core.

It is also notable that the SOA appears to be relatively insoluble in this aqueous solution, even though isolated α-pinene SOA is known to be reasonably hygroscopic[82]. If the solubility of SOA is greatly diminished in mixed composition particles (which pervade the atmosphere) this has significant implications for the CCN activity of these particles; the aqueous solution will be much more dilute at the Köhler maximum in the droplet growth curve under supersaturated conditions than at 80% RH.

The glycerol(aq) plus SOA experiment is especially interesting when taken into the context of the NaCl(aq) plus SOA experiment. First, it shows that in both experiments there is limited solubility of the SOA in the initial droplet phase, leading to the phase separation. Second, both experiments added SOA to an aqueous droplet, but the NaCl(aq) system formed an emulsion in the core whereas the glycerol(aq) core did not. The physical formation of the emulsion is due to SOA particles coagulating onto the surface of the droplet, but that does not explain why it is a stable emulsion as shown in Figure 1. The same coagulation of homogeneously nucleated SOA is occurring with the glycerol(aq) droplet yet for that system SOA promptly starts to form a coating without creating an emulsion. Differences in the ionic strength of the NaCl(aq) versus glycerol(aq) phases and the interfacial energies between the SOA and the two aqueous phases likely explains why a stable emulsion only exists in the NaCl(aq) phase. In the atmosphere, this emulsified state would increase exposed SOA surface area to the aqueous medium and thus give more SOA the opportunity to undergo aqueous chemistry. The prevalence of the SOA emulsion may be limited to high number concentration regimes where coagulational loss on to larger particles is significant, such as new particle formation events that frequently occur, particularly near forested regions with high biogenic VOC emissions[78,83]. It would also delay the formation of a stable core-shell morphology where all the undissolved SOA resides at the air-particle interface. Considering our observations of a stable emulsified state for 48 hours, RH cycling in the atmosphere may play an important role in determining the morphology of mixed SOA and aqueous inorganic particles, and the prevalent atmospheric particle mixing state.

The AOT experiment on the α-pinene SOA coating squalane system refines the interpretation of smog-chamber experiments reported by Robinson et al.[7]. They also observed phase separation of squalane and SOA, which our AOT experiments confirm.

Our experiment provides the additional observation that the phase-separated particle is a core-shell morphology, an important property that was unobservable in the smog chamber experiments. We have determined that a shell of α-pinene SOA surrounding the squalane core is the thermodynamically stable state for this mixture. Now we can definitively interpret the results from the aerosol evaporation experiments performed by Robinson et al. [7]. They observed prompt evaporation of squalane (which is more volatile than the oxidized SOA) which could indicate that the diffusion coefficient of the squalane in SOA phase is sufficiently high to promote the transport of squalane through the SOA as it evaporates. This interpretation requires the SOA to be coating the squalane phase, which our AOT experiments now confirm is the equilibrium morphology. Combining the results from our AOT experiments and their chamber experiments we can conclude that squalane has no major diffusion limitation through α-pinene SOA, at moderate humidity.

In addition to squalane, we also observe glycerol evaporating through an SOA shell in Figure 3. From that experiment, we conclude that glycerol has no major diffusion limitation through α-pinene SOA, at moderate humidity. Finally, from the rapid WGM response to the RH cycle of the SOA coating an NaCl(aq) droplet, we conclude that water also has no major diffusion limitation through α-pinene SOA. The shell thickness of the α-pinene SOA on the glycerol(aq) and NaCl(aq) droplets was 65 nm and 519 nm, respectively, thus there would be minimal diffusion limitations for particles of similar sizes composed only of α-pinene SOA. The smog-chamber mixing experiments of squalane and α-pinene SOA directly probed atmospherically relevant sizes at 5% RH and observed no diffusion limitations through the α-pinene SOA[7]. If these results hold for other OA systems then assuming prompt partitioning under moderate humidities in atmospheric chemical transport models is valid when the model time steps are on the order of minutes[46,53,84–86]. A forthcoming paper will explore in detail the physical properties of the SOA observed from these and additional AOT experiments, such as the volatility, diffusivity, viscosity, and surface tension of the SOA.

Acknowledgements. Kyle Gorkowski was supported in part by a Bertucci Fellowship from Carnegie Mellon University's College of Engineering. This research was supported by the National Science Foundation (Awards CHE-1213718 & CHE-1554941). We thank Jonathan Reid and James Walker at the University of Bristol for valuable discussions regarding the analysis and interpretation of the AOT Raman spectra.

Supporting Information. Includes a detailed schematic of the aerosol optical tweezers experimental system, assessment of the core-shell fitting algorithm, details of the evaporation rate calculation, Raman spectra from a squalane droplet containing solid NaCl crystals, isolated frames of the Raman spectra from the NaCl(aq) plus SOA experiment, and a tabulation of reported refractive index values for α-pinene SOA.

References

(1) Kolb, C. E.; Worsnop, D. R. Chemistry and Composition of Atmospheric Aerosol Particles. *Annu. Rev. Phys. Chem.* **2012**, *63* (1), 471–491.

(2) Pöschl, U. Atmospheric aerosols: composition, transformation, climate and health effects. *Angew. Chem. Int. Ed. Engl.* **2005**, *44* (46), 7520–7540.

(3) Gentner, D. R.; Isaacman, G.; Worton, D. R.; Chan, A. W. H.; Dallmann, T. R.; Davis, L.; Liu, S.; Day, D. A.; Russell, L. M.; Wilson, K. R.; et al. Elucidating secondary organic aerosol from diesel and gasoline vehicles through detailed characterization of organic carbon emissions. *Proc. Natl. Acad. Sci. U. S. A.* **2012**.

(4) Hallquist, M.; Wenger, J. C.; Baltensperger, U.; Rudich, Y.; Simpson, D.; Claeys, M.; Dommen, J.; Donahue, N. M.; George, C.; Goldstein, A. H.; et al. The formation, properties and impact of secondary organic aerosol: current and emerging issues. *Atmos. Chem. Phys.* **2009**, *9* (14), 5155–5236.

(5) Zhang, Q.; Jimenez, J. L.; Canagaratna, M. R.; Allan, J. D.; Coe, H.; Ulbrich, I.; Alfarra, M. R.; Takami, A.; Middlebrook, A. M.; Sun, Y. L.; et al. Ubiquity and dominance of oxygenated species in organic aerosols in anthropogenically-influenced Northern Hemisphere midlatitudes. *Geophys. Res. Lett.* **2007**, *34* (13), L13801.

(6) Surratt, J. D.; Murphy, S. M.; Kroll, J. H.; Ng, N. L.; Hildebrandt, L.; Sorooshian, A.; Szmigielski, R.; Vermeylen, R.; Maenhaut, W.; Claeys, M.; et al. Chemical

Composition of Secondary Organic Aerosol Formed from the Photooxidation of Isoprene. *J. Phys. Chem. A* **2006**, *110* (31), 9665–9690.

(7) Robinson, E. S.; Saleh, R.; Donahue, N. M. Probing the evaporation dynamics of mixed {SOA}/squalane particles using size-resolved composition and single-particle measurements. *Environ. Sci. Technol.* **2015**, *49*, 9724–9732.

(8) Zhao, Y.; Wingen, L. M.; Perraud, V.; Finlayson-Pitts, B. J. Phase, composition, and growth mechanism for secondary organic aerosol from the ozonolysis of alpha-cedrene. *Atmos. Chem. Phys.* **2016**, *16* (5), 3245–3264.

(9) IPCC. *Climate Change 2013: The Physical Science Basis. Contribution of Working Group I to the Fifth Assessment Report of the Intergovern- mental Panel on Climate Change*; Stocker, T.F., D. Qin, G.-K. Plattner, M. Tignor, S.K. Allen, J. Boschung, A. Nauels, Y. Xia, V. Bex, P. M. M., Ed.; Cambridge University Press: Cambridge, 2013.

(10) Pope, C. A.; Ezzati, M.; Dockery, D. W. Fine-particulate air pollution and life expectancy in the United States. *N. Engl. J. Med.* **2009**, *360* (4), 376–386.

(11) Hekayati, J.; Roosta, A.; Javanmardi, J. Liquid–liquid equilibria in the quinary aqueous two-phase system of poly(ethylene glycol) 6000+sodium sulfate+water in the presence of glucose and ethanol: Experimental investigation and thermodynamic modeling. *Thermochim. Acta* **2016**, *625*, 47–52.

(12) Bateman, A. P.; Gong, Z.; Liu, P.; Sato, B.; Cirino, G.; Zhang, Y.; Artaxo, P.; Bertram, A. K.; Manzi, A. O.; Rizzo, L. V.; et al. Sub-micrometre particulate matter is primarily in liquid form over Amazon rainforest. *Nat. Geosci.* **2015**, *9* (1), 34–37.

(13) Song, M.; Marcolli, C.; Krieger, U. K.; Zuend, A.; Peter, T. Liquid-liquid phase separation in aerosol particles: Dependence on O:C, organic functionalities, and compositional complexity. *Geophys. Res. Lett.* **2012**, *39* (19).

(14) You, Y.; Smith, M. L.; Song, M.; Martin, S. T.; Bertram, A. K. Liquid–liquid phase separation in atmospherically relevant particles consisting of organic species and inorganic salts. *Int. Rev. Phys. Chem.* **2014**, *33* (1), 43–77.

(15) Stewart, D. J.; Cai, C.; Nayler, J.; Preston, T. C.; Reid, J. P.; Krieger, U. K.; Marcolli, C.; Zhang, Y.-H. H. Liquid–Liquid Phase Separation in Mixed Organic/Inorganic Single Aqueous Aerosol Droplets. *J. Phys. Chem. A* **2015**, *119* (18), 4177–4190.

(16) Schill, G. P.; Tolbert, M. A. Heterogeneous ice nucleation on phase-separated organic-sulfate particles: Effect of liquid vs. glassy coatings. *Atmos. Chem. Phys.* **2013**, *13* (9), 4681–4695.

(17) Renbaum-Wolff, L.; Song, M.; Marcolli, C.; Zhang, Y.; Liu, P. F.; Grayson, J. W.;

Geiger, F. M.; Martin, S. T.; Bertram, A. K. Observations and implications of liquid–liquid phase separation at high relative humidities in secondary organic material produced by *α*-pinene ozonolysis without inorganic salts. *Atmos. Chem. Phys.* **2016**, *16* (12), 7969–7979.

(18) You, Y.; Bertram, A. K. Effects of molecular weight and temperature on liquid–liquid phase separation in particles containing organic species and inorganic salts. *Atmos. Chem. Phys.* **2015**, *15* (3), 1351–1365.

(19) Song, M.; Marcolli, C.; Krieger, U. K.; Lienhard, D. M.; Peter, T. Morphologies of mixed organic/inorganic/aqueous aerosol droplets. *Faraday Discuss.* **2013**, *165*, 289–316.

(20) Kwamena, N.-O. A.; Buajarern, J.; Reid, J. P. Equilibrium morphology of mixed organic/inorganic/aqueous aerosol droplets: investigating the effect of relative humidity and surfactants. *J. Phys. Chem. A* **2010**, *114* (18), 5787–5795.

(21) Metcalf, A. R.; Boyer, H. C.; Dutcher, C. S. Interfacial Tensions of Aged Organic Aerosol Particle Mimics Using a Biphasic Microfluidic Platform. *Environ. Sci. Technol.* **2016**, *50* (3), 1251–1259.

(22) Buajarern, J.; Mitchem, L.; Reid, J. P. Characterizing multiphase Organic/Inorganic/Aqueous aerosol droplets. *J. Phys. Chem. A* **2007**, *111* (37), 9054–9061.

(23) O'Brien, R. E.; Wang, B.; Kelly, S. T.; Lundt, N.; You, Y.; Bertram, A. K.; Leone, S. R.; Laskin, A.; Gilles, M. K.; O'Brien, R. E.; et al. Liquid–Liquid Phase Separation in Aerosol Particles: Imaging at the Nanometer Scale. *Environ. Sci. Technol.* **2015**, *49* (8), 4995–5002.

(24) Reid, J. P.; Dennis-Smither, B. J.; Kwamena, N.-O. A.; Miles, R. E. H.; Hanford, K. L.; Homer, C. J. The morphology of aerosol particles consisting of hydrophobic and hydrophilic phases: hydrocarbons, alcohols and fatty acids as the hydrophobic component. *Phys. Chem. Chem. Phys.* **2011**, *13* (34), 15559–15572.

(25) Smith, M. L.; You, Y.; Kuwata, M.; Bertram, A. K.; Martin, S. T. Phase transitions and phase miscibility of mixed particles of ammonium sulfate, toluene-derived secondary organic material, and water. *J. Phys. Chem. A* **2013**, *117* (36), 8895–8906.

(26) You, Y.; Renbaum-Wolff, L.; Carreras-Sospedra, M.; Hanna, S. J.; Hiranuma, N.; Kamal, S.; Smith, M. L.; Zhang, X.; Weber, R. J.; Shilling, J. E.; et al. Images reveal that atmospheric particles can undergo liquid-liquid phase separations. *Proc. Natl. Acad. Sci. U. S. A.* **2012**, *109* (33), 13188–13193.

(27) Altaf, M. B.; Freedman, M. A. Effect of Drying Rate on Aerosol Particle

Morphology. *J. Phys. Chem. Lett.* **2017**, *8* (15), 3613–3618.

(28) Veghte, D. P.; Altaf, M. B.; Freedman, M. A. Size dependence of the structure of organic aerosol. *J. Am. Chem. Soc.* **2013**, *135* (43), 16046–16049.

(29) Altaf, M. B.; Zuend, A.; Freedman, M. A. Role of nucleation mechanism on the size dependent morphology of organic aerosol. *Chem. Commun.* **2016**, *52* (59), 9220–9223.

(30) Cai, C.; Tan, S.; Chen, H.; Ma, J.; Wang, Y.; Reid, J. P.; Zhang, Y. Slow water transport in MgSO 4 aerosol droplets at gel-forming relative humidities. *Phys. Chem. Chem. Phys.* **2015**, *17* (44), 29753–29763.

(31) Meresman, H.; Hudson, A. J.; Reid, J. P. Spectroscopic characterization of aqueous microdroplets containing inorganic salts. *Analyst* **2011**, *136* (17), 3487–3495.

(32) Gorkowski, K.; Beydoun, H.; Aboff, M.; Walker, J. S.; Reid, J. P.; Sullivan, R. C. Advanced aerosol optical tweezers chamber design to facilitate phase-separation and equilibration timescale experiments on complex droplets. *Aerosol Sci. Technol.* **2016**, *50* (12), 1327–1341.

(33) Abbatt, J. P. D.; Lee, A. K. Y.; Thornton, J. A. Quantifying trace gas uptake to tropospheric aerosol: recent advances and remaining challenges. *Chem. Soc. Rev.* **2012**, *41* (19), 6555–6581.

(34) Alexander, B.; Hastings, M. G.; Allman, D. J.; Dachs, J.; Thornton, J. A.; Kunasek, S. A. Quantifying atmospheric nitrate formation pathways based on a global model of the oxygen isotopic composition (D17O) of atmospheric nitrate. *Atmos. Chem. Phys.* **2009**, *9* (14), 5043–5056.

(35) Gaston, C. J.; Thornton, J. A. Reacto-Diffusive Length of N2O5 in Aqueous Sulfate- and Chloride-Containing Aerosol Particles. *J. Phys. Chem. A* **2016**, *120* (7), 1039–1045.

(36) Park, S.-C.; Burden, D. K.; Nathanson, G. M. The Inhibition of N2O5 Hydrolysis in Sulfuric Acid by 1-Butanol and 1-Hexanol Surfactant Coatings. *J. Phys. Chem. A* **2007**, *111* (15), 2921–2929.

(37) Surratt, J. D.; Kroll, J. H.; Kleindienst, T. E.; Edney, E. O.; Claeys, M.; Sorooshian, A.; Ng, N. L.; Offenberg, J. H.; Lewandowski, M.; Jaoui, M.; et al. Evidence for Organosulfates in Secondary Organic Aerosol. *Environ. Sci. Technol.* **2007**, *41* (2), 517–527.

(38) Gaston, C. J.; Riedel, T. P.; Zhang, Z.; Gold, A.; Surratt, J. D.; Thornton, J. A. Reactive uptake of an isoprene-derived epoxydiol to submicron aerosol particles.

Environ. Sci. Technol. **2014**, *48* (19), 11178–11186.

(39) Ye, J.; Gordon, C. A.; Chan, A. W. H. Enhancement in Secondary Organic Aerosol Formation in the Presence of Preexisting Organic Particle. *Environ. Sci. Technol.* **2016**, *50* (7), 3572–3579.

(40) Song, C.; Zaveri, R. A.; Shilling, J. E.; Alexander, M. L.; Newburn, M. Effect of hydrophilic organic seed aerosols on secondary organic aerosol formation from ozonolysis of α-pinene. *Environ. Sci. Technol.* **2011**, *45* (17), 7323–7329.

(41) Gordon, C. A.; Ye, J.; Chan, A. W. H. Secondary Organic Aerosol Formation Enhanced by Organic Seeds of Similar Polarity at Atmospherically Relative Humidity. *STEM Fellowsh. J.* **2015**, *1* (2), 6–10.

(42) Lu, J. W.; Rickards, A. M. J.; Walker, J. S.; Knox, K. J.; Miles, R. E. H.; Reid, J. P.; Signorell, R. Timescales of water transport in viscous aerosol: measurements on sub-micron particles and dependence on conditioning history. *Phys. Chem. Chem. Phys.* **2014**, *16* (21), 9819–9830.

(43) Davies, J. F.; Haddrell, A. E.; Miles, R. E. H.; Bull, C.; Reid, J. P. Bulk, Surface and Gas-Phase Limited Water Transport in Aerosol. *J. Phys. Chem. A* **2012**, *116* (45), 10987–10998.

(44) Vaden, T. D.; Imre, D.; Beránek, J.; Shrivastava, M.; Zelenyuk, A. Evaporation kinetics and phase of laboratory and ambient secondary organic aerosol. *Proc. Natl. Acad. Sci. U. S. A.* **2011**, *108* (6), 2190–2195.

(45) Abramson, E.; Imre, D.; Beránek, J.; Wilson, J.; Zelenyuk, A. Experimental determination of chemical diffusion within secondary organic aerosol particles. *Phys. Chem. Chem. Phys.* **2013**, *15* (8), 2983–2991.

(46) Liu, P.; Li, Y. J.; Wang, Y.; Gilles, M. K.; Zaveri, R. A.; Bertram, A. K.; Martin, S. T. Lability of secondary organic particulate matter. *Proc. Natl. Acad. Sci.* **2016**, *113* (45), 12643–12648.

(47) Dennis-Smither, B. J.; Hanford, K. L.; Kwamena, N. O. A.; Miles, R. E. H.; Reid, J. P. Phase, morphology, and hygroscopicity of mixed oleic acid/sodium chloride/water aerosol particles before and after ozonolysis. *J. Phys. Chem. A* **2012**, *116* (24), 6159–6168.

(48) Cai, C.; Stewart, D. J.; Preston, T. C.; Walker, J. S.; Zhang, Y.-H.; Reid, J. P. A new approach to determine vapour pressures and hygroscopicities of aqueous aerosols containing semi-volatile organic compounds. *Phys. Chem. Chem. Phys.* **2014**, *16* (7), 3162–3172.

(49) Rickards, A. M. J.; Miles, R. E. H.; Davies, J. F.; Marshall, F. H.; Reid, J. P. Measurements of the sensitivity of aerosol hygroscopicity and the κ parameter to the O/C ratio. *J. Phys. Chem. A* **2013**, *117* (51), 14120–14131.

(50) Davis, R. D.; Lance, S.; Gordon, J. A.; Ushijima, S. B.; Tolbert, M. A. Contact efflorescence as a pathway for crystallization of atmospherically relevant particles. *Proc. Natl. Acad. Sci.* **2015**, *112* (52), 15815–15820.

(51) Shiraiwa, M.; Zuend, A.; Bertram, A. K.; Seinfeld, J. H. Gas-particle partitioning of atmospheric aerosols: interplay of physical state, non-ideal mixing and morphology. *Phys. Chem. Chem. Phys.* **2013**, *15* (27), 11441–11453.

(52) Presto, A. A.; Donahue, N. M. Investigation of α-Pinene + Ozone Secondary Organic Aerosol Formation at Low Total Aerosol Mass. *Environ. Sci. Technol.* **2006**, *40* (11), 3536–3543.

(53) Donahue, N. M.; Robinson, A. L.; Trump, E. R.; Riipinen, I.; Kroll, J. H.; McNeill, V. F.; Ariya, P. A. Volatility and Aging of Atmospheric Organic Aerosol. *Atmos. Aerosol Chem.* **2014**, *339*, 97–143.

(54) Wills, J. B.; Knox, K. J.; Reid, J. P. Optical control and characterisation of aerosol. *Chem. Phys. Lett.* **2009**, *481* (4–6), 153–165.

(55) Lan, J. J. Y. and M. H. and J. Y. and Y. Z. Surface whispering-gallery mode. *EPL (Europhysics Lett.* **2011**, *96* (5), 57003.

(56) Preston, T. C.; Reid, J. P. Accurate and efficient determination of the radius, refractive index, and dispersion of weakly absorbing spherical particle using whispering gallery modes. *J. Opt. Soc. Am. B-Optical Phys.* **2013**, *30* (8), 2113–2122.

(57) Preston, T. C.; Reid, J. P. Determining the size and refractive index of microspheres using the mode assignments from Mie resonances. *J. Opt. Soc. Am. A* **2015**, *32* (11), 2210–2217.

(58) Song, M.; Marcolli, C.; Krieger, U. K.; Zuend, a.; Peter, T. Liquid-liquid phase separation and morphology of internally mixed dicarboxylic acids/ammonium sulfate/water particles. *Atmos. Chem. Phys.* **2012**, *12* (5), 2691–2712.

(59) Mishchenko, M. I.; Liu, L.; Mackowski, D. W. Morphology-dependent resonances of spherical droplets with numerous microscopic inclusions. *Opt. Lett.* **2014**, *39* (6), 1701.

(60) Ngo, D.; Pinnick, R. G. Suppression of scattering resonances in inhomogeneous microdroplets. *J. Opt. Soc. Am. A* **1994**, *11* (4), 1352.

(61) Voorhees, P. W. The theory of Ostwald ripening. *J. Stat. Phys.* **1985**, *38* (1–2), 231–252.

(62) Nakayama, T.; Sato, K.; Matsumi, Y.; Imamura, T.; Yamazaki, A.; Uchiyama, A. Wavelength Dependence of Refractive Index of Secondary Organic Aerosols Generated during the Ozonolysis and Photooxidation of alpha-Pinene. *Sci. Online Lett. Atmos.* **2012**, *8* (0), 119–123.

(63) Kim, H.; Liu, S.; Russell, L. M.; Paulson, S. E. Dependence of Real Refractive Indices on O:C, H:C and Mass Fragments of Secondary Organic Aerosol Generated from Ozonolysis and Photooxidation of Limonene and α-Pinene. *Aerosol Sci. Technol.* **2014**, *48* (5), 498–507.

(64) Kim, H.; Barkey, B.; Paulson, S. E. Real refractive indices of α- And β-pinene and toluene secondary organic aerosols generated from ozonolysis and photo-oxidation. *J. Geophys. Res. Atmos.* **2010**, *115* (23), 1–10.

(65) Kim, H.; Paulson, S. E. Real refractive indices and volatility of secondary organic aerosol generated from photooxidation and ozonolysis of limonene, alpha-pinene and toluene. *Atmos. Chem. Phys.* **2013**, *13* (15), 7711–7723.

(66) Redmond, H.; Thompson, J. E. Evaluation of a quantitative structure-property relationship (QSPR) for predicting mid-visible refractive index of secondary organic aerosol (SOA). *Phys. Chem. Chem. Phys.* **2011**, *13* (15), 6872–6882.

(67) Wexler, A. S. Atmospheric aerosol models for systems including the ions H+, NH4+, Na+, SO 4 2-, NO3, Cl- , Br- , and H2O. *J. Geophys. Res.* **2002**, *107* (D14), 4207.

(68) Tröstl, J.; Chuang, W. K.; Gordon, H.; Heinritzi, M.; Yan, C.; Molteni, U.; Ahlm, L.; Frege, C.; Bianchi, F.; Wagner, R.; et al. The role of low-volatility organic compounds in initial particle growth in the atmosphere. *Nature* **2016**, *533* (7604), 527–531.

(69) Kroll, J. H.; Ng, N. L.; Murphy, S. M.; Flagan, R. C.; Seinfeld, J. H. Secondary Organic Aerosol Formation from Isoprene Photooxidation. *Environ. Sci. Technol.* **2006**, *40* (6), 1869–1877.

(70) Dommen, J.; Metzger, A.; Duplissy, J.; Kalberer, M.; Alfarra, M. R.; Gascho, A.; Weingartner, E.; Prevot, A. S. H.; Verheggen, B.; Baltensperger, U. Laboratory observation of oligomers in the aerosol from isoprene/NO x photooxidation. *Geophys. Res. Lett.* **2006**, *33* (13), 1–5.

(71) Cai, C.; Stewart, D. J.; Reid, J. P.; Zhang, Y.; Ohm, P.; Dutcher, C. S.; Clegg, S. L. Organic component vapor pressures and hygroscopicities of aqueous aerosol

measured by optical tweezers. *J. Phys. Chem. A* **2015**, *119* (4), 704–718.

(72) Ray, A. K.; Davis, E. J.; Ravindran, P. Determination of ultra-low vapor pressures by submicron droplet evaporation. *J. Chem. Phys.* **1979**, *71* (2), 582–587.

(73) Yli-Juuti, T.; Pajunoja, A.; Tikkanen, O.-P.; Buchholz, A.; Faiola, C.; V?is?nen, O.; Hao, L.; Kari, E.; Per?kyl?, O.; Garmash, O.; et al. Factors controlling the evaporation of secondary organic aerosol from alpha-pinene ozonolysis. *Geophys. Res. Lett.* **2017**, *44* (5), 1–9.

(74) Kampf, C. J.; Waxman, E. M.; Slowik, J. G.; Dommen, J.; Pfaffenberger, L.; Praplan, A. P.; Prévôt, A. S. H.; Baltensperger, U.; Hoffmann, T.; Volkamer, R. Effective Henry's Law Partitioning and the Salting Constant of Glyoxal in Aerosols Containing Sulfate. *Environ. Sci. Technol.* **2013**, *47* (9), 4236–4244.

(75) EPA, U. Estimation Programs Interface Suite™ for Microsoft® Windows. United States Environmental Protection Agency 2012.

(76) Kroll, J. H.; Lim, C. Y.; Kessler, S. H.; Wilson, K. R. Heterogeneous Oxidation of Atmospheric Organic Aerosol: Kinetics of Changes to the Amount and Oxidation State of Particle-Phase Organic Carbon. *J. Phys. Chem. A* **2015**, *119* (44), 10767–10783.

(77) Bateman, A. P.; Nizkorodov, S. a; Laskin, J.; Laskin, A. High-Resolution Electrospray Ionization Mass Spectrometry Analysis of Water-Soluble Organic Aerosols Collected with a Particle into Liquid Sampler. *Anal. Chem.* **2010**, *82* (19), 8010–8016.

(78) Zhang, X.; Dalleska, N. F.; Huang, D. D.; Bates, K. H.; Sorooshian, A.; Flagan, R. C.; Seinfeld, J. H. Time-resolved molecular characterization of organic aerosols by PILS + UPLC/ESI-Q-TOFMS. *Atmos. Environ.* **2016**, *130*, 180–189.

(79) Xu, L.; Guo, H.; Weber, R. J.; Ng, N. L. Chemical Characterization of Water-Soluble Organic Aerosol in Contrasting Rural and Urban Environments in the Southeastern United States. *Environ. Sci. Technol.* **2017**, *51* (1), 78–88.

(80) Stewart, D. J.; Cai, C.; Nayler, J.; Preston, T. C.; Reid, J. P.; Krieger, U. K.; Marcolli, C.; Zhang, Y. H. Liquid–Liquid Phase Separation in Mixed Organic/Inorganic Single Aqueous Aerosol Droplets. *J. Phys. Chem. A* **2015**, *119* (18), 4177–4190.

(81) Davies, J. F.; Miles, R. E. H.; Haddrell, A. E.; Reid, J. P. Influence of organic films on the evaporation and condensation of water in aerosol. *Proc. Natl. Acad. Sci. U. S. A.* **2013**, *110* (22), 8807–8812.

(82) Rothfuss, N. E.; Petters, M. D. Influence of Functional Groups on the Viscosity of

Organic Aerosol. *Environ. Sci. Technol.* **2017**, *51* (1), 271–279.

(83) Herrmann, H.; Schaefer, T.; Tilgner, A.; Styler, S. A.; Weller, C.; Teich, M.; Otto, T. Tropospheric Aqueous-Phase Chemistry: Kinetics, Mechanisms, and Its Coupling to a Changing Gas Phase. *Chem. Rev.* **2015**, *115* (10), 4259–4334.

(84) Tsigaridis, K.; Daskalakis, N.; Kanakidou, M.; Adams, P. J.; Artaxo, P.; Bahadur, R.; Balkanski, Y.; Bauer, S. E.; Bellouin, N.; Benedetti, A.; et al. The AeroCom evaluation and intercomparison of organic aerosol in global models. *Atmos. Chem. Phys.* **2014**, *14* (19), 10845–10895.

(85) Ye, Q.; Robinson, E. S.; Ding, X.; Ye, P.; Sullivan, R. C.; Donahue, N. M. Mixing of secondary organic aerosols versus relative humidity. *Proc. Natl. Acad. Sci.* **2016**, *113* (45), 12649–12654.

(86) Gilardoni, S.; Massoli, P.; Paglione, M.; Giulianelli, L.; Carbone, C.; Rinaldi, M.; Decesari, S.; Sandrini, S.; Costabile, F.; Gobbi, G. P.; et al. Direct observation of aqueous secondary organic aerosol from biomass-burning emissions. *Proc. Natl. Acad. Sci.* **2016**, *113* (36), 10013–10018.